Numerical Simulations of Stellar Convective Dynamos.
I. The Model and Method*

GARY A. GLATZMAIER[†]

*Theoretical Division, Los Alamos National Laboratory,
Los Alamos, New Mexico*

A numerical model used to simulate global convection and magnetic field generation in stars is described. Nonlinear, three-dimensional, time-dependent solutions of the anelastic magnetohydrodynamic equations are presented for a stratified, rotating, spherical, fluid shell heated from below. The velocity, magnetic field, and thermodynamic perturbations are expanded in spherical harmonics to resolve their horizontal structure and in Chebyshev polynomials to resolve their radial structure. An explicit Adams–Bashforth time integration scheme is used with an implicit Crank–Nicolson treatment of the diffusion terms. Nonlinear terms are computed in physical space; and spatial derivatives are computed in spectral space. The resulting second-order differential equations are solved with a Chebyshev collocation method. Preliminary solutions for a Solar-like model are briefly discussed. Convective motions driven in the upper, superadiabatic part of the zone penetrate into the lower, subadiabatic part of the zone. Differential rotation, induced by the interaction of convection and rotation, is an equatorial acceleration at the surface as observed on the Sun; below the surface angular velocity decreases with depth. The meridional circulation and the equator-pole temperature excess are within Solar observational constraints; however, the giant-cell velocities at the surface are larger than observed. The large-scale magnetic field, induced by the differential rotation and helical motions, peaks in the subadiabatic region below the convection zone; and, near the top of the convection zone, it is concentrated over the downdrafts of giant cells. A systematic drift in latitude of the magnetic field or a field reversal has not yet been seen.

I. INTRODUCTION

Many studies of stellar convection have been made via numerical simulations governed by the hydrodynamic or magnetohydrodynamic equations using various approximations and numerical techniques. Nonlinear convection in a spherical shell has been numerically simulated by Durney [1], Young [2], Gilman [3–5], and Marcus [6–8]. These models all employ the Boussinesq approximation for which there is no basic density stratification. However, stellar convection zones have large density stratifications; so the Boussinesq approximation presents a serious limitation.

461

Several models have been developed within the anelastic approximation which enables one to model convection over several density scale-heights without solving the fully compressible equations. Latour, Spiegel, Toomre, and Zahn [9–12], Van der Borght [13, 14], and Massaguer and Zahn [15] have performed nonlinear, anelastic, modal calculations. Their solutions are represented by one or two horizontal planforms in plane parallel geometry with a fine vertical grid resolution. Nordlund [16] has developed a nonlinear, anelastic, multimode convection model including radiative transfer and has had great success in simulating Solar granulation. Another anelastic model, developed by Glatzmaier and Gilman [17–20], has been used to study the interaction of convection and rotation in a stratified, rotating, spherical shell. However, their solutions represented only initial tendencies since the nonlinear terms in the second-order calculations were constructed from the linear solutions of the first-order calculations.

Magnetic fields were not included in the models mentioned above. However, convective flow of ionized stellar gas across magnetic field lines generates time-dependent magnetic fields which produce feedbacks on the flow and on the thermodynamics. Kinematic dynamo models produce magnetic field solutions for a prescribed velocity field. Most of the work on kinematic dynamo theory has incorporated the mean field approximation [21–25]. Yoshimura [26, and references within] has taken kinematic theory a step further with his highly parameterized three-dimensional model. When his fictitious velocity is adequately tuned, the model produces what looks very much like the Solar magnetic cycle. A more consistent, three-dimensional, kinematic model has been developed by Cuong and Busse [27]. Their specified velocity field (in the linear magnetic induction equation) is a highly truncated modal solution of the hydrodynamical equations for a rotating, incompressible, spherical shell.

Several MHD models have been developed that simultaneously solve for the velocity and magnetic fields; that is, the nonlinear MHD equations are solved with the Lorentz force in the momentum equation. The decay of unforced MHD turbulence has been numerically simulated by Orszag and Tang [28] in two dimensions and by Pouquet and Patterson [29] in three dimensions to study the cascade of kinetic and magnetic energy. By solving two-dimensional MHD equations with an externally imposed magnetic field, Peckover and Weiss [30], Galloway and Moore [31], and Weiss [32, 33] have numerically simulated the concentration of magnetic flux into sheets and ropes between convection cells. Dynamo action generated by the interaction of rotation and convection has been numerically simulated with highly truncated modal calculations by Kropachev [34], Soward [35], Baker [36], and Fautrelle and Childress [37], and with multimode calculations for a rotating spherical shell by Gilman [38, 39].

These nonlinear MHD simulations have shed considerable light on many aspects of magnetoconvection and self-excited dynamo action; however, they all have employed the Boussinesq approximation. A. Nordlund (private communication) has recently included magnetic fields in his anelastic Solar granulation model; and P. A. Gilman (private communication) has converted his Boussinesq dynamo code into an

anelastic dynamo. The model described in this paper is also a multimode, nonlinear, dynamic dynamo within the anelastic approximation; it includes the effects of rotation, spherical geometry, density stratification, and penetration into a subadiabatic region. We hope to gain a better understanding of global convection and magnetic field generation in stars by analyzing, with good spatial and temporal resolution, the physics responsible for such phenomena in our numerical simulations. We describe the model in Section II and the numerical method used to solve the equations in Section III. Preliminary solutions for a Solar model are presented in Section IV. Future papers in this series will discuss the solutions and their physical significance in greater detail.

II. THE STELLAR MODEL

We simulate global stellar convection and magnetic field generation by solving the nonlinear, three-dimensional, time-dependent, anelastic magnetohydrodynamic equations for a stratified, rotating, spherical, fluid shell heated from below. The anelastic approximation [17, 40] is valid when the convective velocity is small compared to the local sound speed. This should be the case when the unstable region is only slightly superadiabatic. To first order in an expansion parameter ε representing either the Mach number squared or the superadiabaticity, the divergence of the mass flux vanishes. As a result, sound waves are filtered out. In other words, pressure adjusts instantaneously throughout the fluid as if the sound speed were infinite. Although the time derivative of the density does not appear in the anelastic mass continuity equation, density does vary in space and time and the fluid is compressible but on a convective time-scale not an acoustic time-scale. In addition, we assume the Alfvén velocity scales like the convective velocity. The advantage provided by the anelastic approximation is that convection can be modeled over many density scale-heights with a time-step significantly larger than what would be needed if one were solving the fully compressible equations and forced to temporally resolve sound waves and fast magnetoacoustic waves. Since the stellar convection zones we model have large density stratifications and are very nearly adiabatic and since we hope to study magnetic cycles in these stellar models with periods of the order of tens of years, the anelastic approximation is the obvious choice.

One of our basic assumptions is that the large-scale global structure of the differential rotation and magnetic field in a rotating star is determined mainly by the interaction of large-scale convection and rotation. The Coriolis effect on small-scale eddies should be insignificant since their turnover times are short compared to the rotation period of the star. However, the diffusion of large-scale momentum, entropy, and magnetic flux by these small-scale eddies is much more significant than via radiative or molecular processes. Therefore, in our model we explicitly resolve the structure and time-dependence of a large spectrum of cells while parameterizing the viscous, thermal, and magnetic diffusive effects of the turbulent eddies too small to resolve.

The reference state, about which perturbations are sought, is time independent, only a function of radius, adiabatic to first order, and described relative to a rotating frame. The fluid is assumed to be a fully ionized perfect gas. Centrifugal force is assumed negligible relative to gravitational force. In addition, we assume the viscous $\bar{\nu}$, thermal $\bar{\kappa}$, and magnetic $\bar{\eta}$ eddy diffusivities are scalar functions of radius. The reference state equations of state, momentum, and energy are

$$\bar{p} = R_* \bar{\rho} \bar{\theta} \tag{1a}$$

$$\frac{d\bar{p}}{dr} = -g\bar{\rho}, \qquad g = \frac{GM_*}{r^2} \tag{1b}$$

$$\frac{L_*}{4\pi r^2} = -\bar{\kappa}\bar{\rho}\bar{\theta}\frac{d\bar{s}}{dr} - c_p\bar{\kappa}_r\bar{\rho}\frac{d\bar{\theta}}{dr}. \tag{1c}$$

We are using the same notation as in [17], except here the variables are dimensional. The solution of Eqs. (1a) and (1b) is a polytrope when assuming to first order an adiabatic temperature gradient [17]. The reference state is determined by specifying the stellar mass, luminosity, and rotation rate, the radii of the top and bottom boundaries of the spherical shell, the mean composition of the shell, the temperature and density at the top boundary, and the three eddy diffusivities as functions of radius. Alternatively, we could specify a reference state that is more like one resulting from a mixing-length model instead of using a polytropic stratification.

Equation (1c) states that in the absence of large-scale motion the stellar luminosity is carried partially by the small-scale turbulent heat flux driven by the reference state entropy gradient and partially by the radiative heat flux driven by the reference state temperature gradient. The radiative thermometric diffusivity $\bar{\kappa}_r$ is constructed with the opacity a function of the reference state temperature and density. Then the reference state entropy gradient $d\bar{s}/dr$, which is of order ε, is determined by Eq. (1c). Note that we are assuming both

$$\frac{\bar{\kappa}_r}{\bar{\kappa}} \qquad \text{and} \qquad \frac{\bar{\theta}}{c_p}\frac{d\bar{s}}{dr}\bigg/\frac{d\bar{\theta}}{dr}$$

are of order ε which is a very good assumption for the stellar convection zones we will consider. Also, note that in a subadiabatic region where the entropy gradient is positive the turbulent heat flux is directed downward. This is realistic since fluid motions tend to bring the medium closer to an adiabatic state. That is, they tend to make the temperature gradient less steep in a superadiabatic region and more steep in a subadiabatic region. This formulism of the heat flux differs from the traditional mixing-length approach which assumes no penetration into the subadiabatic region. In mixing-length models $(\nabla - \nabla_{AD})$, which is $(-(H_p/c_p)(d\bar{s}/dr))$, jumps from a very small positive value in the superadiabatic region to a relatively large negative value in the subadiabatic region. In our model the transition is more gradual due to the presence of small-scale eddies generated by large-scale motions penetrating into the subadiabatic region.

In the preliminary calculations we choose to let the eddy diffusivities decrease with depth. This is partly motivated by linear calculations using these diffusivities [19, 20] which produced surface differential rotation profiles in good agreement with Solar observations. Also, an argument made by P. A. Gilman (private communication) based on mixing-length theory provides a physical reason for such a radial dependence. He argues that, although the product of convective velocity and pressure scale-height remains nearly constant in a mixing-length convection model, the mixing-length velocity represents the total convective velocity; whereas, our eddy diffusivities represent only the effect of those scales too small to explicitly resolve in the model. Therefore, since eddies of the order of a pressure scale-height are more easily resolved in the lower part of the zone, our eddy diffusivities should represent a smaller diffusive effect there than near the top of the zone where the pressure scale-height is much smaller. Another argument is based on the entropy gradient. Since the upper part of our shell is superadiabatic whereas the lower part is subadiabatic, the large-scale motions, which generate the eddies, should be much weaker in the lower part of the shell. Consequently, the eddies should have a smaller diffusive effect there. In a future paper we will account for eddy diffusion is a more self-consistent manner by using a subgrid-scale eddy diffusivity.

The anelastic perturbation equations are described in [17] and will be listed here in their dimensional form. Two magnetic field equations have been added along with the Lorentz force in the momentum equation and Joule heating in the entropy equation. Barred variables are reference state variables which are only functions of radius; unbarred variables are perturbations which are functions of radius, colatitude, longitude, and time. Note that the perturbation temperature θ, density ρ, pressure p, and entropy s all include a time-dependent, spherically symmetric component that modifies the time-independent reference state; consequently, the mean state is time-dependent. The perturbations equations of state, mass flux, momentum, entropy, magnetic flux, and magnetic induction are

$$\frac{p}{\bar{p}} = \frac{\rho}{\bar{\rho}} + \frac{\theta}{\bar{\theta}} = \left(\frac{\gamma}{\gamma-1}\right)\left(\frac{\theta}{\bar{\theta}} - \frac{s}{c_p}\right) \tag{2a}$$

$$\nabla \cdot \bar{\rho}\mathbf{v} = 0 \tag{2b}$$

$$\bar{\rho}\frac{\partial \mathbf{v}}{\partial t} = -\nabla p - g\rho\hat{r} + 2\bar{\rho}\mathbf{v}\times\boldsymbol{\Omega} - \nabla\cdot\mathbf{D} + \bar{\rho}\mathbf{v}\times(\nabla\times\mathbf{v})$$

$$- \frac{1}{2}\bar{\rho}\nabla|\mathbf{v}|^2 + \frac{1}{4\pi}(\nabla\times\mathbf{B})\times\mathbf{B} \tag{2c}$$

$$\bar{\rho}\bar{\theta}\frac{\partial s}{\partial t} = \nabla\cdot(\bar{\kappa}\bar{\rho}\bar{\theta}\,\nabla s) - \bar{\rho}\bar{\theta}\mathbf{v}\cdot\nabla(\bar{s}+s)$$

$$+ 2\bar{\nu}\bar{\rho}\left(e_{ij}e_{ij} - \frac{1}{3}(\nabla\cdot\mathbf{v})^2\right) + \frac{1}{4\pi}\bar{\eta}|\nabla\times\mathbf{B}|^2 \tag{2d}$$

$$\nabla\cdot\mathbf{B} = 0 \tag{2e}$$

$$\frac{\partial \mathbf{B}}{\partial t} = \nabla \times (\mathbf{v} \times \mathbf{B}) - \nabla \times (\bar{\eta} \nabla \times \mathbf{B}). \tag{2f}$$

The viscous stress tensor is related to the rate of strain tensor by

$$D_{ij} = -2\bar{\rho}\bar{v} \left(e_{ij} - \frac{1}{3} (\nabla \cdot \mathbf{v}) \, \delta_{ij} \right).$$

Equation (2f) is the result of the MHD approximation for which the electric current density is

$$\mathbf{J} = \frac{1}{4\pi} \nabla \times \mathbf{B}$$

and the electric field is

$$\mathbf{E} = \bar{\eta} \nabla \times \mathbf{B} - \mathbf{v} \times \mathbf{B}.$$

The nondimensional equations [17] contain Rayleigh and Froude numbers which depend on the value of the expansion parameter ε. In [17], ε was chosen to be proportional to the entropy gradient at the top of the convection zone. Instead, one could have chosen it to be proportional to the change in the entropy across the unstable region. However, the precise definition of the expansion parameter used to formally derive the anelastic equations from the fully compressible equations is arbitrary. What is essential for Eqs. (2) to be valid is that the resulting convective and Alfvén velocities be small compared the local sound speed and the thermodynamic perturbations be small relative to their reference state values. This should be the case when the specified change in the reference state entropy across the unstable region is small.

Note that the perturbation diffusive heat flux in Eq. (2d) is driven by the perturbation entropy gradient. This is consistent with the concept of an eddy thermometric diffusivity since the heat liberated by an eddy after moving adiabatically over a mixing-length in pressure equilibrium is proportional to the change in the entropy of the surroundings over that displacement. Note also that the total entropy gradient in Eq. (2d), i.e., the sum of the reference state and the perturbation entropy gradients, appears in the advective term. This follows naturally from the assumption that the reference state entropy gradient is of order ε as mentioned above. As a result, the perturbations grow until the spherically symmetric part of the total entropy gradient in the unstable region becomes as small as it can for the given diffusivities.

A total perturbation energy equation can be constructed by adding the dot product of the velocity and the momentum equation, the entropy equation, and the dot product of the magnetic field and the magnetic induction equation. We assume impermeable, stress-free boundaries; so the rate of change of the total energy of the shell

$$\frac{\partial}{\partial t} \int_V \left(\bar{\rho}\bar{\theta}s + \frac{1}{2} \bar{\rho}v^2 + \frac{1}{8\pi} B^2 \right) dV = \int_S \left(\bar{\kappa}\bar{\rho}\bar{\theta} \, \nabla s - \frac{1}{4\pi} \mathbf{E} \times \mathbf{B} \right) \cdot d\mathbf{S} \tag{3a}$$

is determined by the perturbation heat flux and magnetic energy flux through the boundaries. We require the total radial diffusive heat flux through the bottom boundary to be constant; and we assume the core below the shell is perfectly electrically conducting. Therefore, the surface integral over the bottom boundary in Eq. (3a) vanishes. The choice of boundary conditions at the top is not so obvious. Among the many possibilities, we could require the radial heat flux to be constant or the entropy to be constant over the top boundary. However, when the effect of rotation is significant, the top boundary condition on the entropy perturbation has little effect on the dynamics in the bulk of the convection zone. This was also found to be the case in the linear anelastic calculations [19]. In addition, we will require the magnetic field at the top either to have only a radial component or to be matched to an external potential field. If, at the top boundary, the radial heat flux were required to be constant and the magnetic field only radial the total energy of the shell would remain constant. However, matching to an external potential field is more attractive since the structure and amplitude of the external magnetic field is determined by the field at the top boundary which is known at each time-step. Although, an external potential field exists only in the absence of external currents, which is not case on short time-scales in the stellar atmosphere above the convection zone, such a treatment should result in an approximate simulation of the large-scale structure and evolution of an external magnetic field anchored far below the stellar surface.

The rate of change of the total angular momentum of the shell relative to the rotating frame of reference depends on the Reynolds, Maxwell, and viscous stresses integrated over the boundaries. However, with the above stated boundary conditions, the total stress vanishes at the top and bottom; so the total angular momentum of the shell remains constant:

$$\int_V r \sin \theta \, \bar{\rho} v_\phi \, dV = 0. \tag{3b}$$

Likewise the total mass of the shell remains constant:

$$\int_V \rho \, dV = 0. \tag{3c}$$

III. THE NUMERICAL METHOD

Since the mass flux and the magnetic flux are solenoidal, they can be written as a sum of poloidal and toroidal vectors [41, 42]:

$$\bar{\rho}\mathbf{v} = \nabla \times \nabla \times (W\hat{r}) + \nabla \times (Z\hat{r}) \tag{4a}$$

$$\mathbf{B} = \nabla \times \nabla \times (B\hat{r}) + \nabla \times (J\hat{r}). \tag{4b}$$

That is, Eqs. (2b) and (2e) are exactly satisfied with this formulism. Note that

spherically symmetric radial components, inversely proportional to r^2, formally could be added to (4a) and (4b); however, the impermeable and perfectly electrically conducting bottom boundary conditions do not allow these contributions. Consequently, there are six dependent variables: the defining scalars W and Z for the poloidal and toroidal parts of the mass flux, the defining scalars B and J for the poloidal and toroidal parts of the magnetic field, and the entropy s and pressure p perturbations. The temperature and density perturbations are easily obtained from the perturbation equation of state (2a).

Each of the six functions are expanded in spherical harmonics $Y_l^m(\theta, \phi)$. According to Eq. (4a), the three components of the mass flux take the forms

$$\bar{\rho} v_r = \frac{1}{r^2} \sum_{l,m} l(l+1) \, W_l^m Y_l^m$$

$$\bar{\rho} v_\theta = \frac{1}{r \sin \theta} \sum_{l,m} \left(\frac{\partial W_l^m}{\partial r} \sin \theta \frac{\partial Y_l^m}{\partial \theta} + Z_l^m \frac{\partial Y_l^m}{\partial \phi} \right)$$

$$\bar{\rho} v_\phi = \frac{1}{r \sin \theta} \sum_{l,m} \left(\frac{\partial W_l^m}{\partial r} \frac{\partial Y_l^m}{\partial \phi} - Z_l^m \sin \theta \frac{\partial Y_l^m}{\partial \theta} \right).$$

The radial component of the curl of the mass flux is

$$(\nabla \times \bar{\rho} v)_r = \frac{1}{r^2} \sum_{l,m} l(l+1) \, Z_l^m Y_l^m.$$

Similar expressions exist for the magnetic field in terms of B_l^m and J_l^m.

The complex coefficients of the Y_l^m are further expanded in Chebyshev polynomials. For example:

$$W_l^m(r, t) = \left(\frac{2}{N} \right)^{1/2} \sum_{n=0}^{N} {}'' \, W_{ln}^m(t) \, T_n(r).$$

The double quotes means that the $n = 0$ and $n = N$ terms are multiplied by $\frac{1}{2}$. The radial coordinate r is mapped into coordinate x by

$$x = \frac{2r - r_{\text{top}} - r_{\text{bot}}}{r_{\text{top}} - r_{\text{bot}}}$$

in order to use the Chebyshev mesh-points defined as

$$x_k = \cos \left(\frac{k\pi}{N} \right)$$

with $k = 0$ to N. One could also have incorporated a stretched radial mesh before

mapping to the Chebyshev points. The Chebyshev polynomials evaluated at these x_k are

$$T_n(x_k) = \cos\left(\frac{nk\pi}{N}\right);$$

so the transform from (r, l, m) space to (n, l, m) space is

$$W_{ln}^m(t) = \left(\frac{2}{N}\right)^{1/2} \sum_{k=0}^{N}{}'' W_l^m(x_k, t) \, T_n(x_k).$$

Many properties and techniques of Chebyshev expansions are discussed in [43].

The above expansions are truncated such that

$$0 \leqslant |m| \leqslant l \leqslant L \qquad \text{and} \qquad 0 \leqslant n \leqslant N.$$

When no symmetry is assumed, the six dependent functions are represented by all l and m wave numbers in the above range; so a full spherical shell is modeled. If one required the motion to be symmetric with respect to the equator with no mass flux through the equatorial plane, W_l^m, s_l^m, and p_l^m exist for only even $(l + m)$ and Z_l^m for only odd $(l + m)$. The magnetic field solutions can then be either "dipole-like," with J_l^m existing for only even $(l + m)$ and B_l^m for only odd $(l + m)$, or "quadrupole-like" for which the opposite is true [44]. With these prescribed symmetries, one effectively models a hemispherical shell. One could also prescribe symmetry with respect to a meridian plane by using only even m. We model a full spherical shell and usually set $L = 31$ and $N = 16$ which corresponds to 1024 horizontal modes and 17 radial modes. We explicitly resolve a large spectrum of modes with full nonlinear coupling because highly truncated modal calculations typically produce artificially large temporal variations for systems that are intrinsically time dependent [38].

Spectral methods have been shown to require only half the resolution in each spatial dimension as finite-difference methods to achieve the same accuracy [45, 46]. This apparently is due to the fact that an expansion in orthogonal functions provides information everywhere instead of only at the mesh-points. In addition, all spatial derivatives can be computed exactly in spectral space. Spherical harmonics are the natural expansion functions for a spherical shell problem. Among their many nice properties they do not exhibit the "pole problem" which plagues finite-difference and Fourier series schemes in latitude [47]. That is, due to the convergence of meridian planes near the poles, a much smaller time-step, compared to that required for a spherical harmonic code, must be used for a given resolution unless some mesh-points are filtered out near the poles. Chebyshev polynomials have been chosen because they have a rapid rate of convergence and can easily cope with complicated boundary conditions [43, 48]. In addition, fast Fourier transform algorithms [49] are applicable to Chebyshev transformations and to the longitudinal part of spherical harmonic transformations.

The equations for the complex coefficients of the spherical harmonics are provided

by the anelastic perturbation equations (2). The radial component of the momentum equation, the radial component of the curl of the momentum equation, the entropy equation, the radial component of the induction equation, and the radial component of the curl of the induction equation respectively provide coupled, nonlinear equations for W_l^m, Z_l^m, s_l^m, B_l^m, and J_l^m, each involving a first-order time derivative and a second-order radial derivative. A second-order differential equation for p_l^m, without a time derivative, is obtained from the divergence of the momentum equation using Eq. (2b). Note that this equation is solved after the velocity, entropy perturbation, and magnetic field are calculated for that time-step. This is the essence of what was referred to above as instantaneous pressure adjustments. These equations represent a 17th-order system of differential equations: twelve orders in space and five orders in time. Due to their length, these equations are not displayed here.

A semi-implicit time integration is performed in (r, l, m) space, i.e., in spectral space relative to the horizontal dependence and in physical space relative to the radial dependence. Small random initial conditions are specified for s_l^m and B_l^m; however, we usually do not initialize the B_l^m until the hydrodynamic solution has fully developed. We use an explicit Adams–Bashforth scheme with an implicit Crank–Nicolson treatment of the diffusion terms. Both time integration schemes are second-order accurate. An explicit leap-frog scheme would also be second-order accurate, however it proved to be unconditionally unstable with Chebyshev methods [50]. In addition, the Adams–Bashforth scheme, unlike the leap-frog scheme, does not have a decoupling problem between even and odd time-steps. The Crank–Nicolson scheme was chosen to avoid the stringent radial diffusion restriction on the time-step which would exist for an explicit scheme due to the convergence of the Chebyshev radial mesh-points at the boundaries.

Consider, for example, the equation for s_l^m

$$\frac{\partial s_l^m}{\partial t} = f_l^m + g_l^m \tag{5a}$$

where f_l^m is the diffusion term

$$\bar{\kappa} \left[\frac{\partial^2 s_l^m}{\partial r^2} + \frac{1}{r^2 \bar{\kappa} \bar{\rho} \bar{\theta}} \frac{d}{dr} (r^2 \bar{\kappa} \bar{\rho} \bar{\theta}) \frac{\partial s_l^m}{\partial r} - \frac{l(l+1)}{r^2} s_l^m \right]$$

and g_l^m represents the contribution from the advection, viscous heating, and Joule heating terms. This dynamical equation is approximated by

$$s_{l_{t+\Delta t}}^m - \frac{\Delta t}{2} f_{l_{t+\Delta t}}^m = s_{l_t}^m + \frac{\Delta t}{2} (3g_{l_t}^m - g_{l_{t-\Delta t}}^m + f_{l_t}^m) \tag{5b}$$

where $s_{l_t}^m = s_l^m(r, t)$. Note that when the length of the time-step is changed from Δt_1 to Δt_2 the coefficients of $g_{l_t}^m$ and $g_{l_{t-\Delta t}}^m$ in (5b) should be $(\Delta t_2/2)(2 + \Delta t_2/\Delta t_1)$ and $-(\Delta t_2/2)(\Delta t_2/\Delta t_1)$, respectively.

The five second-order differential equations (in r) resulting from the above stated time differencing scheme together with the second-order differential equation for p_l^m are solved with a Chebyshev collocation method [51–53]. That is, the equations are satisfied at all the Chebyshev radial mesh-points except two in order to satisfy the boundary conditions without over specifying the problem. We choose the points adjacent to the top and bottom boundaries to be the two mesh-points at which the equations are not forced to be satisfied; however, they are very nearly satisfied at these points because the Chebyshev mesh-points converge at the boundaries.

Since only the diffusion terms are treated implicitly, the matrices that require inverting are only $(N + 1)$ by $(N + 1)$, where $(N + 1)$ is the number of Chebyshev polynomials and also the number of Chebyshev mesh-points. There is one matrix equation for each l and m of each of the six dependent functions. However, the matrices that require inverting do not depend on m since $l(l + 1)$ is the eigen-value of the horizontal Laplacian. In addition, they do not depend on time since the reference state is time-independent. Consequently, one matrix for each l of each of the six functions is inverted via LU decomposition are stored. As a result, the matrix equations are easily solved at each time-step by simple matrix multiplications.

Each of the six second-order differential equations for each l and m requires two boundary conditions. The impermeable boundary condition forces W_l^m to vanish at the top and bottom. The stress-free boundary condition forces

$$\frac{\partial^2 W_l^m}{\partial r^2} - \frac{1}{r^2 \bar{\rho}} \frac{dr^2 \bar{\rho}}{dr} \frac{\partial W_l^m}{\partial r} = 0 \qquad \text{and} \qquad \frac{\partial Z_l^m}{\partial r} - \frac{1}{r^2 \bar{\rho}} \frac{dr^2 \bar{\rho}}{dr} Z_l^m = 0$$

at the top and bottom. Since there are four boundary conditions on each W_l^m and only two are required, two conditions are indirectly satisfied via pressure boundary conditions. That is, p_l^m and its radial derivative at the boundaries at time t are forced to be whatever is required to satisfy the extra boundary conditions on W_l^m at time $t + \Delta t$.

To accomplish this, only part of the diffusion term in the equation for W_l^m is treated implicitly. Consider the equation for W_l^m

$$\frac{\partial W_l^m}{\partial t} = \bar{v} \left[\frac{\partial^2 W_l^m}{\partial r^2} + \left(2 \left(\frac{1}{\bar{v}} \frac{d\bar{v}}{dr} + \frac{1}{3\bar{\rho}} \frac{d\bar{\rho}}{dr} + \frac{1}{r} \right) - \frac{1}{r^2 \bar{\rho}} \frac{dr^2 \bar{\rho}}{dr} \right) \frac{\partial W_l^m}{\partial r} \right.$$

$$- \left(\frac{4}{3} \left(\frac{1}{\bar{\rho}} \frac{d\bar{\rho}}{dr} \left(\frac{1}{r} - \frac{1}{\bar{\rho}} \frac{d\bar{\rho}}{dr} \right) + \frac{1}{\bar{\rho}} \frac{d^2 \bar{\rho}}{dr^2} + \frac{1}{\bar{v}} \frac{d\bar{v}}{dr} \left(\frac{3}{r} + \frac{1}{\bar{\rho}} \frac{d\bar{\rho}}{dr} \right) \right)$$

$$\left. + \frac{l(l + 1)}{r^2} \right) W_l^m \right] + g_l^m \tag{6a}$$

where g_l^m represents the contribution from the pressure gradient, buoyancy, Coriolis, Reynolds stress, and Lorentz terms. The semi-implicit time integration scheme for this equation is

$$W^m_{l_{t+\Delta t}} - \frac{\Delta t\, \bar{v}}{2} \left[\frac{\partial^2 W^m_l}{\partial r^2} - \frac{1}{r^2 \bar{\rho}} \frac{dr^2 \bar{\rho}}{dr} \frac{\partial W^m_l}{\partial r} \right.$$

$$- \left(\frac{4}{3} \left(\frac{1}{\bar{\rho}} \frac{d\bar{\rho}}{dr} \left(\frac{1}{r} - \frac{1}{\bar{\rho}} \frac{d\bar{\rho}}{dr} \right) + \frac{1}{\bar{\rho}} \frac{d^2\bar{\rho}}{dr^2} + \frac{1}{\bar{v}} \frac{d\bar{v}}{dr} \left(\frac{3}{r} + \frac{1}{\bar{\rho}} \frac{d\bar{\rho}}{dr} \right) \right) \right.$$

$$\left. \left. + \frac{l(l+1)}{r^2} \right) W^m_l \right]_{t+\Delta t}$$

$$= W^m_{l_t} + \frac{\Delta t}{2} \left(3 \left[g^m_l + 2\bar{v} \left(\frac{1}{\bar{v}} \frac{d\bar{v}}{dr} + \frac{1}{3\bar{\rho}} \frac{d\bar{\rho}}{dr} + \frac{1}{r} \right) \frac{\partial W^m_l}{\partial r} \right]_t \right.$$

$$- \left[g^m_l + 2\bar{v} \left(\frac{1}{\bar{v}} \frac{d\bar{v}}{dr} + \frac{1}{3\bar{\rho}} \frac{d\bar{\rho}}{dr} + \frac{1}{r} \right) \frac{\partial W^m_l}{\partial r} \right]_{t-\Delta t} + \bar{v} \left[\frac{\partial^2 W^m_l}{\partial r^2} - \frac{1}{r^2 \bar{\rho}} \frac{dr^2 \bar{\rho}}{dr} \frac{\partial W^m_l}{\partial r} \right.$$

$$- \left(\frac{4}{3} \left(\frac{1}{\bar{\rho}} \frac{d\bar{\rho}}{dr} \left(\frac{1}{r} - \frac{1}{\bar{\rho}} \frac{d\bar{\rho}}{dr} \right) + \frac{1}{\bar{\rho}} \frac{d^2\bar{\rho}}{dr^2} + \frac{1}{\bar{v}} \frac{d\bar{v}}{dr} \left(\frac{3}{r} + \frac{1}{\bar{\rho}} \frac{d\bar{\rho}}{dr} \right) \right) \right.$$

$$\left. \left. \left. + \frac{l(l+1)}{r^2} \right) W^m_l \right]_t \right). \tag{6b}$$

The boundary conditions on p^m_l and its derivative at time t are such to force the right-hand side of (6b) to vanish at the boundaries and the conditions on W^m_l at time $t + \Delta t$ are that it vanishes at the boundaries. As a result, both the impermeable and stress-free boundary conditions are satisfied.

The equation for s^m_l also requires two boundary conditions for each l and m. If one requires the heat flux to be constant through a boundary, the perturbation radial diffusive flux must vanish there; that is, $\partial s^m_l / \partial r$ must vanish at that boundary. If s^m_l is forced to vanish at a boundary the total entropy remains constant there.

The boundary conditions on the magnetic field are satisfied via conditions on B^m_l and J^m_l. A perfectly conducting bottom boundary requires the radial component of the magnetic field and the horizontal component of the electric field to vanish there. Since the radial component of the velocity also vanishes there, the horizontal component of the current density vanishes at the bottom. Consequently,

$$B^m_l = \frac{\partial^2 B^m_l}{\partial r^2} = \frac{\partial J^m_l}{\partial r} = 0$$

at the bottom. However, as pointed out by P. H. Roberts (private communication), only the second and third of these are required since the first automatically vanishes at the bottom when v_r and B_r vanish there due to the radial component of the induction equation assuming B^m_l was initially zero at the bottom. The two remaining conditions on B^m_l and J^m_l are applied at the top. If the magnetic field is required to have only a radial component at the top, then

$$\frac{\partial B^m_l}{\partial r} = J^m_l = 0$$

at the top boundary. If, on the other hand, the magnetic field at the top is matched to an external potential field that decreases at least as fast as r^{-3} as $r \to \infty$, then

$$\frac{\partial B_l^m}{\partial r} + \frac{l B_l^m}{r} = J_l^m = 0$$

at the top boundary; and the external magnetic field is determined by setting (for $r \geqslant r_{\text{top}}$)

$$B_l^m = (r^l B_l^m)_{\text{top}} \, r^{-l} \qquad \text{and} \qquad J_l^m = 0.$$

To illustrate the Chebyshev collocation method we use, consider again Eq. (5b). The Chebyshev expansion of s_l^m, as described above, is

$$s_l^m(x_k, t) = \left(\frac{2}{N}\right)^{1/2} \sum_{n=0}^{N}{}'' s_{ln}^m(t) \, T_n(x_k)$$

where x_k are the Chebyshev radial mesh-points. Substituting this into Eq. (5b)

$$\left(\frac{2}{N}\right)^{1/2} \sum_{n=0}^{N}{}'' \left[T_n - \frac{\Delta t \, \bar{\kappa}}{2} \left(\frac{d^2 T_n}{dr^2} + \frac{1}{r^2 \bar{\kappa} \bar{\rho} \bar{\theta}} \frac{d}{dr} (r^2 \bar{\kappa} \bar{\rho} \bar{\theta}) \frac{dT_n}{dr} - \frac{l(l+1)}{r^2} T_n \right) \right] s_{ln}^m(t + \Delta t)$$

$$= s_{l_t}^m + \frac{\Delta t}{2} (3 g_{l_t}^m - g_{l_{t-\Delta t}}^m + f_{l_t}^m). \tag{7a}$$

As mentioned above, Eq. (7a) is only used for $(N-1)$ Chebyshev points so the boundary conditions can be applied. If, for example, we require $\partial s_l^m / \partial r$ to vanish at the bottom and s_l^m to vanish at the top, the following conditions must be satisfied:

$$\sum_{n=0}^{N} (-1)^n \, n^2 s_{ln}^m = 0 \qquad \text{and} \qquad \sum_{n=0}^{N} s_{ln}^m = 0. \tag{7b}$$

The matrix equation constructed from (7a) for $(N-1)x_k$ together with (7b) can be written as

$$A_{kn} X_n = B_k. \tag{7c}$$

The $(N+1)$ by $(N+1)$ matrix A_{kn} is independent of m and time; the vector B_k is known at time t; and the vector X_n is the solution s_{ln}^m in Chebyshev space at time $t + \Delta t$. As mentioned above, the LU decomposition of A_{kn} is stored so Eq. (7a) is solved at each time-step by simple matrix multiplication. Note that, whenever Δt or $\bar{\kappa}$ is changed, new LU decompositions must be performed. An advantage of this method [52] over one that attempts to solve the equation in (n, l, m) space is that the coefficients on both sides of (7a), which are complicated functions of radius, do not have to be transformed to Chebyshev space and used to evaluate products of functions of

radius. Also, it is not disadvantage to end up in (n, l, m) space after solving (7c) because the first and second-order radial derivatives of s_l^m need to be evaluated. The Chebyshev coefficients of these derivatives are easily evaluated in (n, l, m) space by a backward recurrence relation [43]. Then these functions are transformed to (r, l, m) space with a fast Fourier transform.

There are three functions, p_0^0, s_0^0, and Z_1^0, which require special consideration with regard to conservation of mass, energy, and angular momentum. The spherically symmetric part of the radial component of the momentum equation provides a first-order differential equation for p_0^0. We solve this equation using the Chebyshev collocation method with the equation satisfied at all Chebyshev radial mesh-points except the center one. There we apply conservation of mass, Eq. (3c), as an integral condition using (2a) after s_0^0 has been determined for that time-step.

Conservation of energy and angular momentum, Eqs. (3a) and (3b), will not be satisfied exactly due to truncation errors. However, one could ensure that these equations are satisfied at each time-step at the expense of not exactly satisfying the dynamic equations for s_0^0 and Z_1^0 at one of the inner Chebyshev points. That is, slight adjustments are made in $s_0^0(r)$ and $Z_1^0(r)$ at each step to ensure conservation of energy and angular momentum. The Chebyshev collocation method is used as before but with the extra integral condition replacing the dynamic equation at the center Chebyshev point. The integral condition on $s_0^0(r)$ is determined from Eq. (3a) after the spherically symmetric parts of the kinetic and magnetic energies are calculated for that time-step together with the change in the total energy which depends on the heat and magnetic flux through the boundaries. The integral condition on $Z_1^0(r)$ is determined from Eq. (3b). Comparison runs with and without these integral conditions on s_0^0 and Z_1^0 have produced negligible differences.

Now consider the nonlinear terms. At each time-step we transform our functions to physical space (r, θ, ϕ), perform the nonlinear multiplication, and transform back to (r, l, m) space. It has been shown [54–56] that this method is significantly faster than evaluating vector-coupled sums directly in spectral space. The Legendre transform in colatitude is performed via a Gaussian quadrature and the Fourier transform in longitude is performed via an FFT.

We use $2(N + 1)(L + 1)^2$ Chebyshev–Legendre–Fourier mesh-points in physical space; so the spectral representation of nonlinear terms is aliased. An unaliased method, which would require significantly more computer time and memory, would ensure that the error due to the truncation of harmonics is normal to the retained set of harmonics. However, a truncation error still would exist at each time-step as it does for the aliased method. If the two methods produce solutions that are not negligibly different, both solutions are bad. Only when enough harmonics are retained so both methods produce negligibly different solutions are the solutions good [53, 57].

Another aspect of the computation of nonlinear terms should be mentioned. We compute terms in the p_l^m, Z_l^m, B_l^m, and J_l^m equations involving the divergence, the radial component of the curl, and the radial component of the curl of the curl of a nonlinear vector in the following way. (Note that, by using Eq. (2b), the advective

term in Eq. (2d) could also be written as a divergence of a nonlinear vector.) Only the functions required to compute a nonlinear vector $\mathbf{F}(r, \theta, \phi)$ are transformed to physical space. Then, the functions

$$f_1 = r^2 F_r, \qquad f_2 = \frac{F_\theta}{r \sin \theta}, \qquad f_3 = \frac{F_\phi}{r \sin \theta},$$

which are calculated at all the Chebyshev–Legendre–Fourier mesh-points, are transformed to (r, l, m) space. The desired spherical harmonic coefficients are then computed according to the formulas

$$(\mathbf{\nabla} \cdot \mathbf{F})_l^m = \left[\frac{1}{r^2} \frac{\partial f_{1_l}^m}{\partial r} + (l+1) c_l^m f_{2_{l-1}}^m - l c_{l+1}^m f_{2_{l+1}}^m + im f_{3_l}^m \right]$$

$$(\mathbf{\nabla} \times \mathbf{F})_{r_l}^m = \left[(l+1) c_l^m f_{3_{l-1}}^m - l c_{l+1}^m f_{3_{l+1}}^m - im f_{2_l}^m \right]$$

$$(\mathbf{\nabla} \times \mathbf{\nabla} \times \mathbf{F})_{r_l}^m = \frac{1}{r^2} \left[\frac{l(l+1)}{r^2} f_{1_l}^m + \frac{\partial}{\partial r} \left(r^2 ((l+1) c_l^m f_{2_{l-1}}^m - l c_{l+1}^m f_{2_{l+1}}^m + im f_{3_l}^m) \right) \right]$$

where

$$c_l^m = \left(\frac{(l+m)(l-m)}{(2l+1)(2l-1)} \right)^{1/2} \qquad \text{and} \qquad i = (-1)^{1/2}.$$

The radial derivatives are obtained by transforming the functions to Chebyshev space, calculating the coefficients of the derivatives, and transforming back to (r, l, m) space. A similar procedure was proposed in [2]; however, an additional recursive operation is required for that procedure.

To maintain numerical stability, we require Δt, at every time-step, to be less than

$$\left. \left| \frac{\Delta r}{f} \right| \right|_{\mathrm{MIN}}, \qquad \left. \left| \frac{\Delta r}{v_r} \right| \right|_{\mathrm{MIN}}, \qquad \left. \left| \frac{r}{\sqrt{L(L+1)(v_\theta^2 + v_\phi^2)}} \right| \right|_{\mathrm{MIN}}. \tag{8}$$

The first of these limits is the radial diffusion time limit; where f is the explicit part of the viscous diffusion term in Eq. (6b). The last two are the radial and horizontal CFL advection time limits.

On the Cray computer, using vectorized do-loops with $L = 31$ and $N = 16$, one time-step requires about 1.7 seconds of cpu. Without the magnetic fields, a time-step requires about one second cpu. The cpu time is approximately proportional to $L^2 N$.

IV. Preliminary Solutions

We will briefly describe solutions for a model that is similar in many ways to the Sun. A rotating, polytropic reference state was constructed based on a standard Solar model. The top boundary was set at 93% of the Solar radius; and the depth of our

zone, including the subadiabatic region, was set at 40% of the radius of the top boundary. There are seven pressure scale-height across this spherical shell. We had the thermal $\bar{\kappa}$, viscous $\bar{\nu}$, and magnetic $\bar{\eta}$ eddy diffusivities decrease with depth inversely proportional to $\bar{\theta}(r)^{0.8}$; and we typically set them, in the center of the zone, to 7×10^{12} cm^2/s, 6×10^{12} cm/s, and 3×10^{12} cm^2/s, respectively. A Kramer opacity was used to construct the radiative thermal diffusivity $\bar{\kappa}_r$; so, with the polytropic reference state, $\bar{\kappa}_r$ increased with depth proportional to $\bar{\theta}(r)^2$. As discussed above, Eq. (1c) is valid if the ratio $\bar{\kappa}_r/\bar{\kappa}$ is small. This ratio varied from approximately 10^{-5} at the bottom of the zone to 10^{-8} at the top.

The MHD solutions described here had a Reynolds number (ratio of maximum fluid velocity to viscous diffusion velocity) of about 50, a magnetic Reynolds number (ratio of maximum fluid velocity to magnetic diffusion velocity) of about 100, and a Hartmann number (ratio of the maximum Alfvén velocity to magnetic and viscous diffusion velocity) of about 5. A maximum, nonaxisymmetric velocity of about 100 m/s usually occurred near the top boundary. This is ten times larger than the observational upper limit on Solar giant-cell velocities. The peak magnetic field at the top boundary was typically 100 gauss which, at our resolution, agrees fairly well with large-scale magnetic field observations on the Sun. The equator-pole temperature excess at the top boundary was about five orders of magnitude smaller than the average surface temperature and therefore within Solar observational constraints. As discussed above, the anelastic approximation is valid if the ratios of the thermodynamic perturbations to their respective reference state values and the square of the ratios of the fluid velocity to the sound speed and the Alfvén velocity to the sound speed are small. For our solutions, these numbers were typically 10^{-5}.

The reference state $\nabla - \nabla_{AD}$ is plotted in Fig. 1 (the upper curve) and defines the superadiabatic and subadiabatic regions of the reference (initial) state. As discussed above, this profile depends on the specification of $\bar{\kappa}$. When a subgrid-scale eddy diffusivity is implemented, the subadiabatic part of the curve in the lower part of the zone probably will be much more negative than that depicted in Fig. 1. A typical profile of the spherically symmetric part of the evolved $\nabla - \nabla_{AD}$ (reference state plus perturbation) is also plotted in Fig. 1 (the lower curve) and illustrates how convection tends to make the state adiabatic, especially in the unstable region where the convection is strong. The two curves meet at the boundaries because constant heat flux boundary conditions were applied.

Kinetic energy, magnetic energy, and entropy variance spectra are plotted versus the longitudinal wave number m at one particular time-step in Fig. 2. The spectra are symmetric about $m = 0$ because, although the functions are expanded in complex spherical harmonics, they must be real functions. The peak in the energy spectra at $m = 0$ is primarily due to the relatively large axisymmetric toroidal fields; whereas the secondary peak is the result of the favored aspect ratio (horizontal to radial dimensions). The secondary peak also appears in energy spectra from nonlinear Boussinesq calculations [3, 38, 39]. However, for a given zone depth and rotation rate, the peak occurs at a larger wave number when there is a density stratification [18–20]. This peak near $m = 15$ for the kinetic energy and entropy variance also
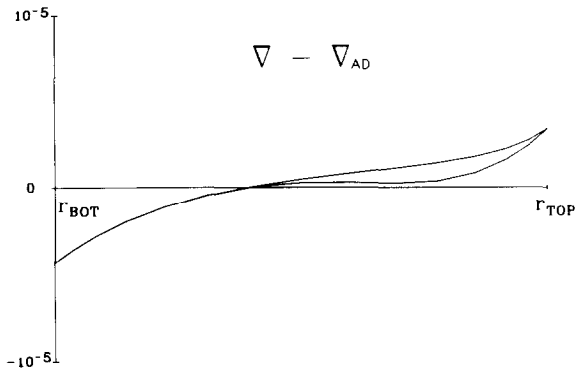
FIG. 1. The initial $\nabla - \nabla_{AD}$ (upper curve) and the evolved $\nabla - \nabla_{AD}$ (lower curve) plotted vs. radius.
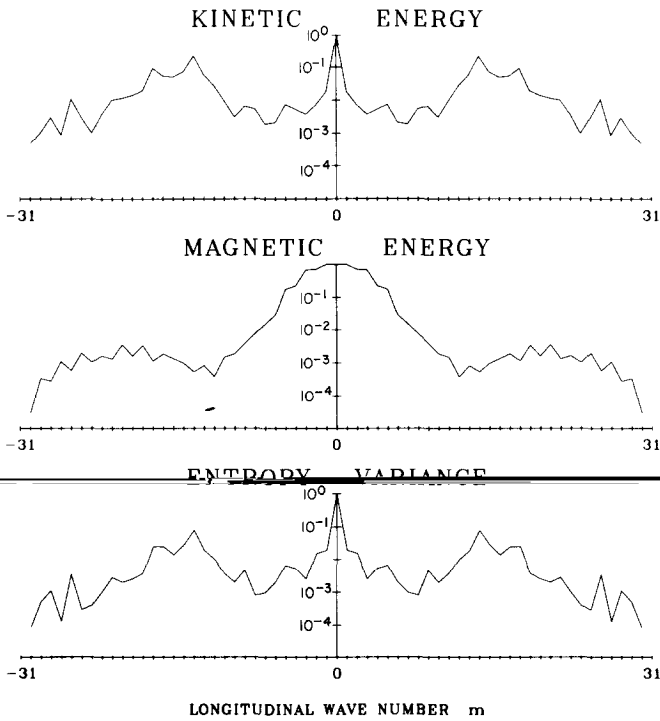

FIG. 2. Kinetic energy, magnetic energy, and entropy variance plotted vs. longitudinal wave number m.

existed when we used $L = 15$. We increased L to 31 so the energy in the smallest scale longitudinal mode would be about three orders of magnitude smaller than the energy in the axisymmetric ($m = 0$) mode, as can be seen in Fig. 2. The kinetic energy, magnetic energy, and entropy variance depend on the horizontal (spherical harmonic) wave number l in a similar way; and they drop monotonically several orders of magnitude with radial (Chebyshev) wave number n. The total magnetic energy is about three orders of magnitude smaller than the total kinetic energy.

A typical profile of mass flux (velocity times density) in the equatorial plane is illustrated in Fig. 3. (Note that the points plotted in these figures do not correspond to the computational mesh-points. Since the solutions are stored in spectral space, we are free to choose any plotting resolution in physical space.) Penetration (convective overshooting) into the stable, subadiabatic, lower part of the zone is evident. Sometimes the downdraft velocities are larger than the surrounding updraft velocities as illustrated at 325° longitude in Fig. 3. However, we have not seen the dramatic downdraft plume structure simulated by fully compressible, non-rotating, two-dimensional, plane-parallel calculations (Toomre [58]). The effect of rotation probably inhibits the plume structure in our three-dimensional simulations. The amount of overshooting depends on how the eddy diffusivities and $\nabla - \nabla_{AD}$ vary in radius. The velocity profile near the bottom of the zone is mainly a shear of the longitudinal velocity; however, small amplitude magnetogravity waves are excited in the stable region by the convective overshooting.

Contours are plotted in Fig. 4 of the radial components of the giant-cell velocity and large-scale magnetic field in a spherical surface just below the top boundary. As one would expect, the convergence of the velocity over downdrafts (the broken contours in the top plot of Fig. 4) tends to concentrate both polarities of the radial magnetic field (bottom plot in Fig. 4). A similar effect, on a granulation scale, has been numerically simulated by A. Nordlund (private communication).
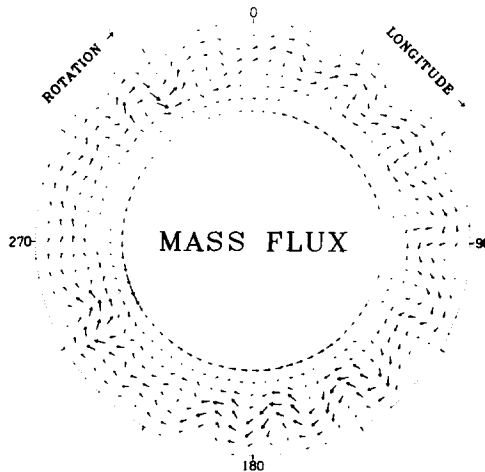

Fig. 3.   Mass flux vectors plotted in the equatorial plane.

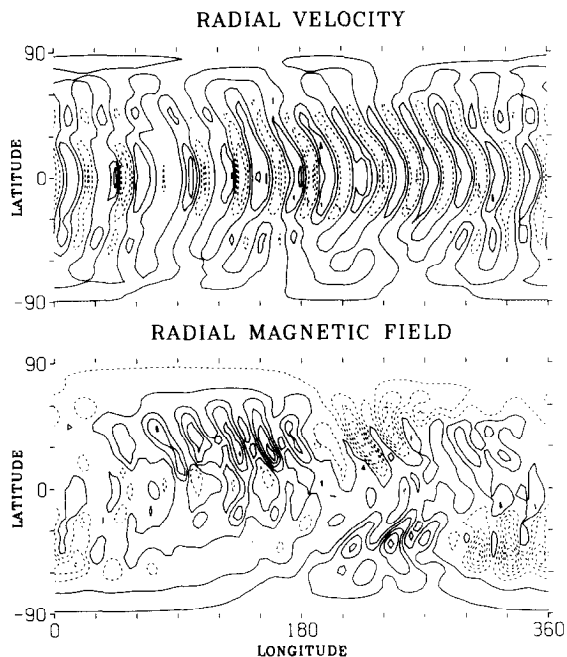RADIAL VELOCITY

RADIAL MAGNETIC FIELD

FIG. 4. Contours of the radial components of the velocity (upper plot) and the magnetic field (lower plot) in a spherical surface just below the top boundary. Solid (broken) contours represent outward (inward) directed fields. The zero contour is solid.

Finally, we have averaged the velocity and magnetic fields in longitude at one particular time-step and plotted, in Fig. 5, their resulting axisymmetric toroidal and poloidal components in a meridian plane. The differential rotation (contours of angular velocity relative to the rotating frame of reference) is plotted in the upper left. It has approximately the same equatorial acceleration at the top boundary as that observed on the Sun. As found in previous nonlinear Boussinesq calculations [3–5, 38, 39] and linear anelastic calculations [20], angular velocity tends to decrease with depth when a broad surface equatorial acceleration is maintained. (Note that Yoshimura [26] specifies an angular velocity that increases with depth in his kinematic dynamo model.) The meridional circulation (streamlines of mass flux) is plotted in the upper right of Fig. 5. In agreement with Solar observations, its direction at the top boundary is poleward and its kinetic energy is about two orders of magnitude smaller than that of the differential rotation. Contours of the toroidal magnetic field (the longitudinal component) are plotted in the lower left of Fig. 5 and the lines of force of the poloidal magnetic field in the lower right. The magnetic field at the top boundary has been matched to an external potential field. These plots show that the magnetic field is stronger in the stable region below the convection zone; however, this picture may be somewhat artificial since the field has not yet fully developed.
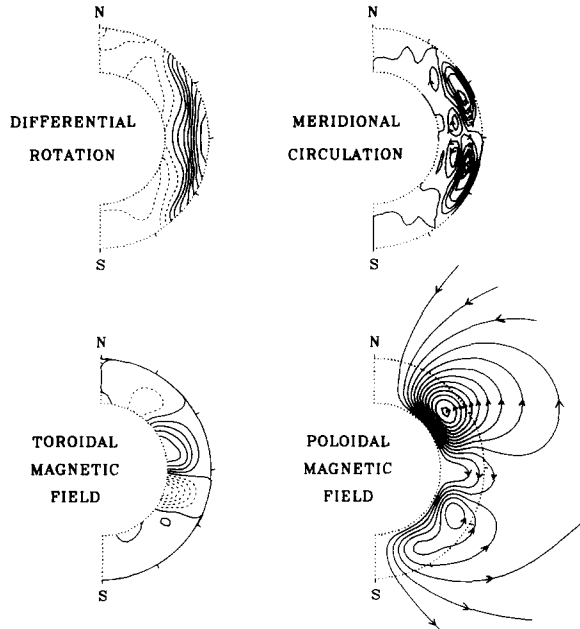
FIG. 5. Longitudinally averaged fields plotted in a meridian plane: contours of angular velocity relative to the rotating frame of reference (upper left), streamlines of the poloidal mass flux (upper right), contours of the toroidal magnetic field (lower left), lines of force of the poloidal magnetic field (lower right). Solid (broken) contours represent fields in the direction of increasing (decreasing) longitude.

One point should be emphasized. The streamlines of mass flux and the magnetic lines of force plotted in Fig. 5 are not the actual streamlines or lines of force, but only those corresponding to the poloidal components of the longitudinally averaged velocity and magnetic fields. The actual lines representing the computed mass flux and magnetic flux are truly three-dimensional and quite complicated.

One can easily see, in Fig. 5, how the toroidal magnetic field has been generated from the poloidal field by the differential rotation. Consider, for example, the northern hemisphere. At low latitude the radial differential rotation shears the poloidal field lines producing a toroidal field in the direction of increasing longitude (solid contours); while at high latitude the radial shear produces a toroidal field in the direction of decreasing longitude (broken contours). Presumably the helical fluid motions generate poloidal fields from toroidal fields [59]; however, we have not yet seen a systematic drift in latitude of the magnetic field or a field reversal.

Kinematic dynamo theory predicts that these magnetic structures will propagate in latitude away from the equator in disagreement with the observed Solar cycle because, in our solutions, angular velocity decreases with depth and helicity (the dot product of velocity and the curl of velocity) is negative in the northern hemisphere and positive in the southern hemisphere. If this occurs, as it has in Gilman's Boussinesq dynamo calculations [39], we will have to re-examine the physics we have and the physics we have not included in our model.

V. SUMMARY

We have proposed a method for studying global convection and magnetic field generation in stars by numerically simulating a self-excited, convective dynamo. The velocity, magnetic field, and thermodynamic perturbations are dynamically consistent solutions of the nonlinear, three-dimensional, time-dependent, anelastic, magneto-hydrodynamic equations. Our model includes the effects of rotation, spherical geometry, density stratification, and penetration into a subadiabatic region. A 17th-order system of equations is integrated in time with a semi-implicit scheme and solved at each time-step with a collocation method. Typically 34816 Chebyshev–Legendre–Fourier mesh-points are used in physical space.

We are quite satisfied with the spherical harmonic and Chebyshev polynomial expansions. As mentioned above, we set L to 31 so the energy in the smallest scale longitudinal mode would be about three orders of magnitude smaller than the energy in the axisymmetric mode. In order to check and evaluate the Chebyshev method, we compared this code with two other versions. One version replaced the Chebyshev expansions and derivatives with a centered second-order finite difference scheme in radius; the other replaced them with a fourth-order finite difference scheme mapped to a stretched radial grid to achieve better resolution near the top where the scale-height becomes small. Treating the diffusion terms implicitly require solving tri-diagonal matrix equations for the second-order scheme and penta-diagonal matrix equations for the fourth-order scheme. All three versions produced results that converged to the same solution as the number of radial mesh-points were increased. However, at least twice as many mesh-points were required for the fourth-order finite difference scheme to achieve the same accuracy as the Chebyshev method; and at least four times as many mesh-points were required for the second-order scheme. As mentioned above, similar results were reported in previous evaluations of spectral methods [45, 46]. The Chebyshev solutions with $N = 16$ were within 2% of those with $N = 64$ after 300 time steps.

We are also satisfied with the semi-implicit Adams–Bashforth–Crank–Nicolson time integration scheme. The time-step limitations (8) were usually sufficient to prevent numerical instabilities (see further comments below); and decreasing Δt by a factor of four produced virtually the same solutions. We also compared this semi-implicit code to a fully explicit version and found that, for the same Δt, the semi-implicit version was more accurate, as on might expect.

One problem that appeared in all versions of the code (Chebyshev, finite difference, semi-implicit, fully explicit) was that if the initial state were made too unstable the energy would grow so fast that the entropy gradient eventually would become subadiabatic everywhere except near the top where the boundary condition forced it to remain superadiabatic. Consequently, convection would be damped everywhere except just below the top boundary. This would produce large viscous heating near the top which would make the rest of the zone become even more subadiabatic. As a result, the scale of convection quickly would become too small to resolve and a numerical instability would develop. This problem exists because we have a top

boundary that forces the radial velocity to vanish instead of a subadiabatic region. Resolving the thin subadiabatic region below the Solar surface would require many more radial mesh-points than would be feasible even with a stretched grid. In our model, the Solar luminosity at the top boundary is essentially all carried by the small-scale eddies parameterized via the eddy thermometric diffusivity. We learned to avoid the numerical instability by not making the state too unstable initially and by maintaning a larger eddy thermometric diffusivity near the top boundary.

Although our model is rich in physics and degrees of freedom, it lacks several ingredients that may (or may not) be essential for simulating a stellar convective dynamo. Instead of solving the fully compressible equations, we have assumed that the convective and Alfvén velocities will be small compared to the local sound speed in order to employ the anelastic approximation which filters out sound waves. We have placed a spherical boundary at the top of our convection zone, below the ionization zones, through which heat and magnetic energy can flow but not mass or angular momentum. We have assumed that our star is not rapidly rotating so centrifugal force will be negligibly small compared to gravitational force and our reference state will be spherically symmetric. The temperature in the zone has been assumed to be low enough to ignore radiation pressure and energy density but high enough to assume a fully ionized perfect gas. The mean molecular weight and the stellar mass and luminosity of the reference state have been assumed independent of radius. The diffusion of heat, momentum, and magnetic flux has been represented by eddy diffusion with specified scalar diffusivities that depend only on radius. Radiative heat flux has been treated within the diffusion approximation using time-independent opacities.

We do not feel that the above assumptions and approximations will severely limit our attempt to gain a better understanding of global stellar convection and dynamo action; however, we intend to improve our model in the future by treating some of these problems more realistically. One deficiency of the model, that may be significant, is its inability to resolve very small-scale, intermittent magnetic flux tubes like those observed on the Solar surface. Although small-scale turbulent eddies presumably induce reconnection by stretching and deforming magnetic field lines, large magnetic flux may be concentrated into thin flux ropes between these eddies in a star. Our model is capable of resolving intricate global magnetic structure; but very small-scale flux ropes will not be simulated due to the effect of the magnetic eddy diffusivity and the truncation of spherical harmonics. Therefore, only global magnetic fields, averaged over length-scales smaller than the limit of our resolution, will be explicitly represented and not the eventual shredding and concentration into intermittent flux tubes observed on the Solar surface.

Our preliminary MHD solutions for a Solar-like model have differential rotation, meridional circulation, large-scale magnetic fields, and an equator-pole temperature excess in fairly good agreement with Solar observations. However, the giant-cell velocities at our top boundary are larger than observed on the Solar surface. This may be due to poor choices for the three eddy diffusivities or not being able to resolve enough pressure scale-heights near the surface. On the other hand, maybe the

large-scale convective velocities quickly degenerate into small-scale velocities near the Solar surface due to the decreasing scale-height and the rapidly increasing superadiabatic gradient; or maybe the time dependence of the large-scale velocity structure has so far prevented good Solar observations of giant-cells.

REFERENCES

1. B. DURNEY, *Astrophys. J.* **161** (1970), 1115.
2. R. E. YOUNG, *J. Fluid Mech.* **63** (1974), 695.
3. P. A. GILMAN, *Geophys. Astrophys. Fluid Dyn.* **8** (1977), 93.
4. P. A. GILMAN, *Geophys. Astrophys. Fluid Dyn.* **11** (1978), 157.
5. P. A. GILMAN, *Geophys. Astrophys. Fluid Dyn.* **11** (1978), 181.
6. P. S. MARCUS, *Astrophys. J.* **231** (1979), 176.
7. P. S. MARCUS, *Astrophys. J.* **239** (1980), 622.
8. P. S. MARCUS, *Astrophys. J.* **240** (1980), 203.
9. J. LATOUR, E. A. SPIEGEL, J. TOOMRE, AND J.-P. ZAHN, *Astrophys. J.* **207** (1976), 233.
10. J. TOOMRE, J.-P. ZAHN, J. LATOUR, AND E. A. SPIEGEL, *Astrophys. J.* **207** (1976), 545.
11. J. LATOUR, J. TOOMRE, AND J.-P. ZAHN, *Astrophys. J.* **248** (1981), 1081.
12. J. LATOUR, J. TOOMRE, AND J.-P. ZAHN, *Solar Phys.* **82** (1983), 387.
13. R. VAN DER BORGHT, *Mon. Not. Roy. Astr. Soc.* **173** (1975), 85.
14. R. VAN DER BORGHT, *Mon. Not. Roy. Astr. Soc.* **188** (1979), 615.
15. J. M. MASSAGUER AND J.-P. ZAHN, *Astron. Astrophys.* **87** (1980), 315.
16. A. NORDLUND, *Astron. Astrophys.* **107** (1982), 1.
17. P. A. GILMAN AND G. A. GLATZMAIER, *Astrophys. J. Suppl.* **45** (1981), 335.
18. G. A. GLATZMAIER AND P. A. GILMAN, *Astrophys. J. Suppl.* **45** (1981), 351.
19. G. A. GLATZMAIER AND P. A. GILMAN, *Astrophys. J. Suppl.* **47** (1981), 103.
20. G. A. GLATZMAIER AND P. A. GILMAN, *Astrophys. J.* **256** (1982), 316.
21. A. M. SOWARD AND P. H. ROBERTS, *Magnit. Girodinamika* **12** (1976), 3; *Magnetohydrodynamics* **12** (1977), 1 [Engl.].
22. H. K. MOFFATT, "Magnetic Field Generation in Electrically Conducting Fluids," Cambridge Univ. Press, Cambridge, 1978.
23. E. N. PARKER, "Cosmical Magnetic Fields," Oxford Univ. Press (Clarendon) Oxford, 1979.
24. M. STIX, *Solar Phys.* **74** (1981), 79.
25. F. KRAUSE AND K.-H. RÄDLER, "Mean Field Magnetohydrodynamics and Dynamo Theory," Pergamon, Oxford, 1981.
26. H. YOSHIMURA, *Astrophys. J. Suppl.* **52** (1983), 363.
27. P. G. CUONG AND F. H. BUSSE, *Phys. Earth Plan. Int.* **24** (1981), 272.

28. S. A. ORSZAG AND C.-M. TANG, *J. Fluid Mech.* **90** (1979), 129.

29. A. POUQUET AND G. S. PATTERSON, *J. Fluid Mech.* **85** (1978), 305.

30. R. S. PECKOVER AND N. O. WEISS, *Mon. Not. Roy. Astr. Soc.* **182** (1978), 189.

31. D. J. GALLOWAY AND D. R. MOORE, *Geophys. Astrophys. Fluid Dyn.* **12** (1979), 73.

32. N. O. WEISS, *J. Fluid Mech.* **108** (1981), 247.

33. N. O. WEISS, *J. Fluid Mech.* **108** (1981), 273.

34. E. P. KROPACHEV, *Geomag. Aeron.* **11** (1971), 585.

35. A. M. SOWARD, *Phil. Trans. Roy. Soc. London A* **275** (1974), 611.

36. L. BAKER, *Geophys. Astrophys. Fluid Dyn.* **9** (1978), 257.

37. Y. FAUTRELLE AND S. CHILDRESS, *Geophys. Astrophys. Fluid Dyn.* **22** (1982), 235.

38. P. A. GILMAN AND J. MILLER, *Astrophys. J. Suppl.* **46** (1981), 211.

39. P. A. GILMAN, *Astrophys. J. Suppl.* **53** (1983), 243.

40. D. O. GOUGH, *J. Atmos. Sci.* **26** (1969), 448.

41. E. C. BULLARD AND H. GELLMAN, *Philos. Trans. Roy. Soc. London A* **247** (1954), 213.

42. S. CHANDRASEKHAR, "Hydrodynamic and Hydromagnetic Stability," Oxford Univ. Press, London, 1961.

43. L. FOX AND I. B. PARKER, "Chebyshev Polynomials in Numerical Analysis," Oxford Univ. Press, London, 1968.

44. P. H. ROBERTS AND M. STIX, *Astron. Astrophys.* **18** (1972), 453.

45. S. A. ORSZAG, *J. Fluid Mech.* **49** (1971), 75.

46. J. R. HERRING, S. A. ORSZAG, R. H. KRAICHNAN, AND D. G. FOX, *J. Fluid Mech.* **66** (1974), 417.

47. S. A. ORSZAG, *Mon. Weath. Rev.* **102** (1974), 56.

48. S. A. ORSZAG, *Phys. Rev. Lett.* **26** (1971), 1100.

49. J. W. COOLEY AND J. W. TUKEY, *Math. Comp.* **19** (1965), 297.

50. D. GOTTLIEB AND S. A. ORSZAG, "Numerical Analysis of Spectral Methods," SIAM, CBMS-NSF, Monograph No. 26, Philadelphia, 1977.

51. C. W. CLENSHAW AND H. J. NORTON, *Comput. J.* **6** (1963), 88.

52. K. WRIGHT, *Comput. J.* **6** (1964), 358.

53. S. A. ORSZAG, *Stud. Appl. Math.* **51** (1972), 253.

54. S. A. ORSZAG, *J. Atmos. Sci.* **27** (1970), 890.

55. E. ELIASEN, B. MACHENHAUER, AND E. RASMUSSEN, "On a Numerical Method for Integration of the Hydrodynamical Equations with a Spectral Representation of the Horizontal Fields," Report No. 2, Institut for Teoretisk Meteorologi, University of Copenhagen, 1970.

56. B. MACHENHAUER AND E. RASMUSSEN, "On the Integration of the Spectral Hydrodynamical Equations by a Transform Method," Report No. 3, Institut for Teoretisk Meteorologi, University of Copenhagen, 1972.

57. D. G. FOX AND S. A. ORSZAG, *J. Comput. Phys.* **11** (1973), 612.

58. J. TOOMRE, *in* "Pulsations in Classical and Cataclysmic Variable Stars," p. 170, (J. P. Cox and C. J. Hansen, eds.), JILA, Boulder, 1982.

59. E. N. PARKER, *Astrophys. J.* **122** (1955), 293.